Gravimetric characterization of Pyrite carbothermic reduction in the presence of lime

O. K. Ilunga[1*], O. T. Johnson[1], F. P. L Kavishe[1], K. K. Alaneme[2]

[1]University of Namibia, Faculty of Agriculture Engineering & Natural Sciences, School of Engineering & built Environment, Department of Mechanical and Metallurgical Engineering, Oshana, Namibia, Tel: +264652324000, Fax: +26488528466 P. O. Box 3624, Namibia, oilunga@unam.na
[2]Federal University of Technology, Department of Metallurgical and materials Engineering Akure, Nigeria, kkalaneme@futa.edu.ng

ABSTRACT

Pyrite, often discarded due to its high sulphur content, holds potential for iron production if processed efficiently. This study investigated the carbothermic reduction of pyrite concentrate (40.75 % iron, 48.04 % sulphur, 0.11 % copper) from the Otjihase Mine in Namibia in the presence of lime, aiming to achieve iron metallization without traditional catalysts while minimizing sulphur emissions. The study examined thermal decomposition, ion exchange, and carbothermic reduction, with mass percent reduction as the key indicator. A factorial experimental design was employed, considering time and C/CaO ratio as independent variables at five levels and temperature at three levels in a reducing environment. The extent of metallization was assessed using mass percent reduction, and data analysis was conducted using ANOVA. Results showed that thermal decomposition led to the highest metallization, while ion exchange effectively captured sulphur. Carbothermic reduction exhibited temperature-dependent trends, with metallization decreasing at 1273K and 1473K but increasing at 1373K. A higher carbon-to-lime ratio enhanced metallization, confirming the critical role of the reducing agent. These findings highlight a viable, environmentally friendly approach to utilizing pyrite for iron production, with potential industrial applications. Further research should focus on optimizing process parameters and assessing large-scale feasibility.

Keywords
Carbothermic; gravimetric; iron; metallization; pyrite; thermal decomposition.

Received: January 2024
Received in revised form: June 2024
Accepted: October 29, 2025
Published: October 31, 2025

1. INTRODUCTION

Pyrite (FeS_2) is the most abundant sulphide mineral, occurring in various geological environments and often associated with valuable metals such as copper, gold, zinc, and lead (Jacobs, 2014; Zhang, 2022). Its primary industrial application lies in sulphuric acid production, with global combined sulphur and pyrite production reaching approximately 80 million tonnes in 2019 (Kutney, 2023; Maslin, 2022). A study reported that 95% of sulphur can be removed at 1503 K after 15 min through sulphides decomposition and oxidation, as well as sulphate decomposition and formation. (Chun, 2011; Denis, 2015). Sponge iron was produced after roasting at 1073 K and Carbothermic reduction of the cinders at 1373 K using coal, (Kama, 2021). This metallization was assessed through the conversion factor ($\boldsymbol{\alpha}$) as shown in Eq. (1); and the mass loss was attributed to direct reduction of haematite and the Boudouard reaction Eq. (2).

$$\alpha = \frac{W_o - W_t}{W_o} \quad (1)$$

$$C + CO_2 = 2CO \qquad \Delta G = 170700 - 174.46T \text{ Jmol}^{-1} \quad (2)$$

Where W_o is the initial mass of the samples and W_t the mass at time t.
The main carbothermic reduction reaction was represented by Eq. (3) and carbon dioxide was stable at 1273K:

$$Fe_2O_3 + 3C = 2Fe + 3CO \qquad \Delta G = 493750 - 452.9T\ Jmol^{-1} \tag{3}$$

Through the process, the net consumption of heat and outward flow of gases through the product influenced the porosity, thermal conductivity, and local reaction rates (Sun, 2009).
However, pyrite and its by-products, such as cinders, are often landfilled, contributing to environmental pollution and resource wastage (Jiang, 2020; Lu, 2022). The need for sustainable utilization of these materials has driven interest in their potential application in ironmaking.

The use of pyrite and cinders in iron production remains limited due to their high sulphur and non-ferrous metal content, which adversely affects product quality (Liu, 2011; Liu, 2012; Qiang, 2019). Sulphur removal is essential for improving iron quality, and this can be achieved either through roasting or by capturing sulphur as calcium sulphide (CaS) using lime, thus preventing harmful SO_2 emissions (Alpi, 2009, Rath, 2017; Vandana, 2015; Zorya, 2015). The introduction of lime also leads to calcium sulphate formation, which reduces the melting point and increases the presence of liquid phases at high temperatures, potentially impeding reaction kinetics (Abzalov, 2008; James, 2013).

Previous studies have demonstrated that iron metallization from complex sulphides ($FeS_2, Cu_5FeS_4, Cu_2S, CuCo_2S_4$) from two different sites (Baluba and Nkana), can be achieved through ion exchange and carbothermic reduction. The copper contents for the two sites were 22.41% and 7.88% respectively, while their pyrite contents were 15.5% and 9%. The extent of metallization was deduced from the mass percent reduction in Eq. (4), where the theoretical mass loss includes: the CO gas in Eq. (5), assuming a complete reaction as well as the mass loss from the volatile species.

$$\%\ \text{Reduction at any time} = \frac{\text{Mass loss at any time}}{\text{Theoretical mass loss}} \times 100 \tag{4}$$

$$MS(sl) + CaO + C = M(s,l) + CaS(s) + CO(g) \tag{5}$$

The mass percent reduction of the ion exchange stage are plotted against time (Figures 1a and 1b), while the carbothermic reduction are plotted in Figures 2a and 2b. The study established in both ion exchange and carbothermic reduction, that the weight loss increased with increasing temperature. For ion exchange reactions the mass loss was attributed to the evolution of $\mathbf{SO_2}$ and volatiles species such as water, in addition, the fast growth of the mass loss at the bigining was mainly due to the thermal decomposition. which is a firrst order reaction (Li, 2015; Tian, 2022) before the ion exchange reaction ini . Furthermore, weight losses recorded were higher than the weight of volatile species and this was explained by the excessively higher amount of sulphur dioxide ($\mathbf{SO_2}$) gas evolved.

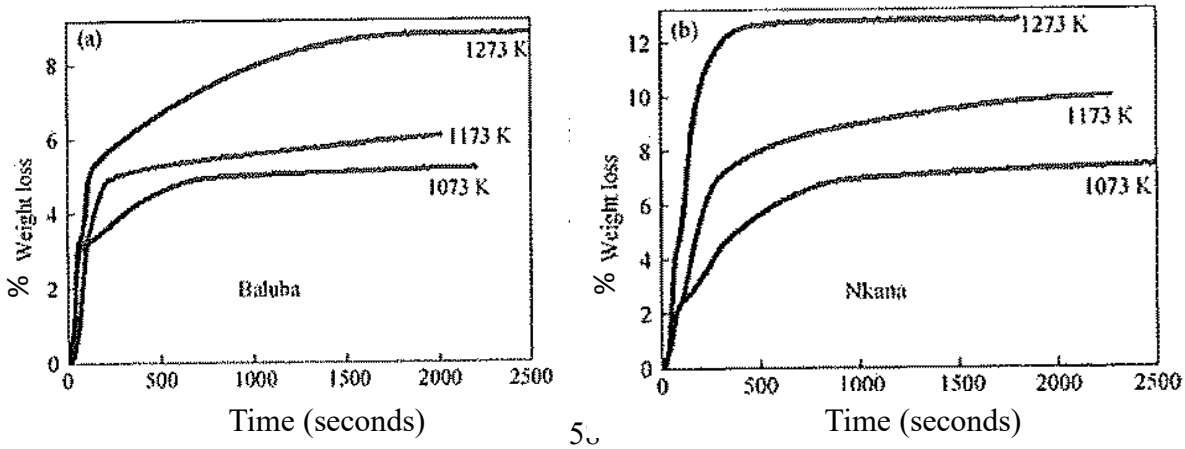

Figure 1. Plots of weight loss against time at various temperatures during mineral sulphides concentrates-lime reaction; (a) Baluba site sample at MS: CaO = 1:2. [23]; (b) Nkana site sample at MS: CaO = 1:2. (Hara, 2014)

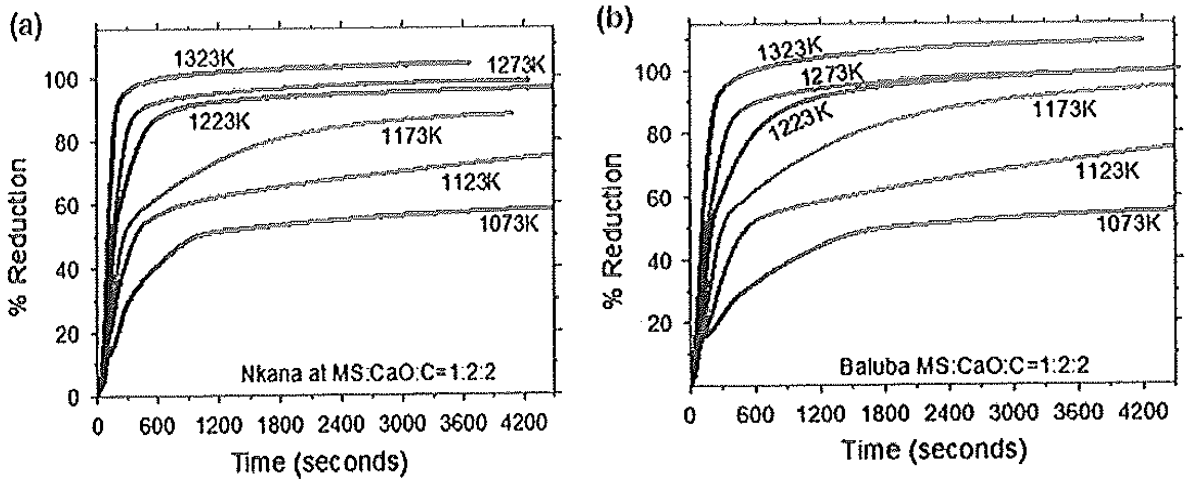

Figure 2. Effect of temperature during reduction of mineral sulphides concentrate in the presence of lime and carbon; (a) Nkana site sample at MS: CaO: C=1:2:2 [25]; (b) Baluba site sample at MS: CaO: C=1:2:2 (Hara, 2013)

However, these investigations have primarily focused on sulphide systems containing non-ferrous metals such as copper and cobalt, particularly chalcocite (Cu_2S), which has been identified as a catalyst that facilitates the reduction process (Hara, 2013; Hara, 2014). Despite these advances, there is a notable gap in the literature concerning the metallization of high-purity pyrite without the catalytic influence of non-ferrous phases. Understanding the behavior of pyrite in a controlled reducing environment without external catalytic effects is critical for determining its suitability as an alternative iron source. Ion exchange is characterized by reactions (6), (7) and (8).

$$4.5FeS_2 + 8\,CaO = 1.5Fe_3O_4 + 8CaS + SO_2 \qquad \Delta G_{1273\,K} = -433\ kJ \tag{6}$$

$$FeS + CaO = FeO + CaS \qquad \Delta G_{1273K} = -55.5kJ \tag{7}$$

$$2.625S_2 + 3.5CaO = 3.5\,CaS + 1.75\,SO_2 \quad \Delta G_{1273\,K} = -168\ kJ \tag{8}$$

The carbothermic stage, the mass percent reductions graphs are characterized by three regimes at temperatures below 1323 K: The first corresponding to thermal decomposition, the second corresponds to combined ion–exchange and carbothermic reduction and the third to carbothermic reduction alone, as shown in Figures 2a and 2b. From the pgaph, in the first regime the curve grows sharply, in the second regime, the curve changes direction and in the third regime the curve is much flatter and decaying further. The first regime covers 20% where mass is rapidly lost due to thermal decomposition of $CuFeS_2$ and FeS_2 as show reactions (9) and (10). Thermal decomposition is also favoured by the presence of iron oxides between 773 and 973 K according to reaction (11).

$$5CuFeS_2 = Cu_5FeS_4 + 4FeS + S_2 \tag{9}$$

$$FeS_2 = FeS + 0.5S_2 \qquad \Delta G = -164.2\ kJ \tag{10}$$

$$2FeS_2 + 3Fe_3O_4 = 4Fe_2O_3 + FeS + \frac{1}{2}S_2 \tag{11}$$

The study suggests that the distilled sulphur from the thermal decomposition is captured by CaO to give CaS and CO gas according to reaction (12).

$$CaO + 0.5S_2 + C = CaS + CO(g) \tag{12}$$

Since the Baluba site sample has more than 40 wt.% $CuFeS_2 + FeS_2$ minerals, the first regime is much clearer for the Baluba site sample than Nkana site sample. The second regime is chemically represnted by reactions (13) and (14).

$$MS(s,l) + CaO(s) = MO(s,l) + CaS(s) \quad (13)$$

Metal oxide is considered as intermediate phase, it is transformed in reducing environment into metal through reaction (14), in the case of iron represented by equations (15), (16), (17) and (18) whenever carbon and heamatite are present in the samples (Ahindra,2008)

$$MO(s,l) + C(s)/CO(g) = M(s,l) + CO/CO_2(g) \quad (14)$$

$$Fe_3O_4 + 4CO = 3Fe + 4CO_2 \quad (15)$$

$$3Fe_2O_3\ (s) + CO\ (g) = 2Fe_3O_4(s) + CO_2\ (g)\ \Delta G = -44.300 - 39.89T\ \ J.mol^{-1} \quad (16)$$

$$Fe_3O_4\ (s) + CO\ (g) = 3FeO(s) + CO_2\ (g)\ \Delta G = 29.86 - 38.29T\ \ J.mol^{-1} \quad (17)$$

$$FeO\ (s) + CO\ (g) = Fe(s) + CO_2\ (g) \qquad \Delta G = -22.8 - 24.26T\ \ J.mol^{-1} \quad (18)$$

The carbon dioxide from reaction (10) reacts with carbon through Boudouard reaction (2) to form carbon monoxide again.

In the second regime, the ion-exchange is faster than the reduction reaction this causes a build-up of metal oxide layer around the unreacted core making the third regime simple direct and indirect reduction of metal oxide. In the presence of lime and carbon, the main reaction of the iron metallization is represented by reaction (19)

$$FeS + CaO + C = Fe + CaS + CO \qquad \Delta G_{1273K} = -55.6kJ \quad (19)$$

Wustite might combine during the process to sulphur dioxide as show equation (20)

$$4.5FeO + 0.75SO_2 = 1.5Fe_3O_4 + 0.375\ S_2 \qquad \Delta G_{1273K} = -50.3\ kJ \quad (20)$$

Earlier literatures reported pyrite conversion into metallic iron (metallization), considering pyrite as part of copper concentrate, characterized as complex sulphide minerals, based on its copper, cobalt, and iron content. Chalcocite (Cu_2S) has played synergetic and catalytic role as it favored the metallization, by forming the intermediate phase calciovolborthite (Ca_2CuFeO_3S); these types of reactions are mostly expected in pyrometallurgy of copper and cobalt (Hara, 2013; Hara, 2014).

However, this study attempted to apply same reduction mechanisms to pyrite concentrate and pyrite cinders which, are high grade iron and sulphur phases, having limited nonferrous concentrations, the study test the null hypothesis: “there is no significant metallization of pyrite in the case where it does not contain of nonferrous”. The extent of reaction could determine the applicability of the process to iron extraction from pyritic deposits such the Otjihase Mine’s, which provided the samples for the study. One way to assess the metallization was to determine the mass variation or conduct gravimetric analysis during the course of reaction. Therefore, this paper presents the finding of the iron metallization from an isolated high grade pyrite concentrate in which nonferrous are in negligible amount using the gravimetric aspect of the process.

This study investigates the carbothermic reduction of high-grade pyrite concentrate obtained from the Otjihase Mine in Namibia, with a focus on its gravimetric characterization. A key aspect of this research is the incorporation of lime (CaO) into the reduction process, which serves as both a desulphurization agent and a flux to capture sulphur as calcium sulphide (CaS) rather than releasing it as SO_2 gas. Unlike traditional roasting methods that result in SO_2 emissions and require further treatment, the lime-assisted reduction approach offers an environmentally friendly alternative by immobilizing sulphur within the solid residue.

The novelty of this study lies in its systematic evaluation of pyrite metallization under controlled conditions, isolating the effects of temperature, reaction time, and the CaO-to-carbon ratio on mass percent reduction. By eliminating the influence of catalytic non-ferrous metals, this research provides a clearer understanding of the direct reduction pathways of pyrite and the

role of lime in enhancing process efficiency. Additionally, the study explores the potential of utilizing pyrite-derived iron as an alternative feedstock for the iron and steel industry while addressing environmental concerns associated with pyrite disposal.

2. MATERIALS AND METHODS

2.1. Sample Collection and Preparation

Pyrite concentrate samples were collected from long-term stockpiles at the Otjihase concentration plant in Namibia. To ensure a systematic and representative sampling process, a simplification of the boundary condition was applied, whereby the stockpile heaps were approximated as trapezoidal geometric shapes with dimensions of 15 m in length, 5 m in height, and 7 m in width, resulting in a total surface area of 188 m². This approach facilitated the estimation of total sample volume and ensured uniform sampling. The sizing of the heaps was carried out based on a partitioning method where the total stockpile was divided into a 1 m × 1 m grid system. This partitioning allowed for systematic sampling across the entire heap to ensure homogeneity and representativeness. Increments were extracted from each grid, with 188 × 350 g increments systematically collected and combined for further processing.

The extracted increments underwent homogenization by thorough mixing, followed by drying under controlled conditions to remove moisture content. Subsequently, the homogenized sample was subjected to rolling to prevent segregation of particles, ensuring a uniform distribution of fine and coarse particles before further processing. Screening was then performed to separate any oversized particles, and a particle size analysis was conducted to determine the granulometric distribution of the sample. The particle size analysis confirmed a P_{84}value of 37.75 µm, indicating that 84% of the sample was finer than this size. The elemental composition of the pyrite concentrate was determined using a handheld X-ray fluorescence (XRF) analysis (TITAN BRUKER), manufactured by Bruker Corporation in Germany**. The results are shown in Table 1. The sample was then divided into seven portions, each weighing 150 g, for subsequent experimental treatments.**

Table 1. Elemental Analysis of the Initial Pyrite Sample

Sample ID	Cu (%)	Fe (%)	Zn (%)	As (%)	S (%)
Otjihase Pyrite	0.11	40.75	0.47	<0.01	48.04

2.2. Sample Blending and Experimental Categorisation

The seven portions of 150 g each were blended with varying ratios of 98% CaO (lime) and 56% C (coal, 150 µm particle size) and analysed, the results of these analysis are represented in Table 2 while the masses that were considered for each reactant are represented in Table 3. The blending process followed a mass balance approach, ensuring the appropriate stoichiometry for sulphur removal and iron metallization. The

number of moles of carbon was computed from the carbon content in coal, while the number of moles of CaO was determined from its lime composition. The mineralogical composition of the original pyrite sample, after blending, was determined as well and is represented in Table 4. The C/CaO ratio was subsequently calculated and considered as a variable for reaction kinetics.

Table 2. Compositions of blended pyrite, lime and coal corresponding to 150 g of each category

Category No	Mg	Si	S	Ca	Mn	Fe	Co	Ni	Cu
1	7.042	1.807	48.04	0.756		42.097	0.084	0.020	0.125
2	5.139	1.442	33.613	14.601		34.909	0.066	0.017	0.093
3	2.143	2.082	35.398	17.214	0.057	36.711	0.103	0.019	0.055
4	1.072	1.964	37.094	15.664	0.028	39.656	0.051	0.032	0.080
5	3.578	1.901	37.915	10.688	0.054	41.132		0.032	0.115
6	5.213	1.571	31.291	17.640	0.039	33.883	0.024	0.024	0.081
7	6.627	1.468	33.241	18.969	0.044	32.330	0.075	0.010	0.081

The blended samples were divided into three main categories based on thermal treatment objectives:

- **Category 1: Thermal decomposition of pyrite**
- **Category 2: Ion exchange reaction**
- **Categories 3–7: Carbothermic reduction with varying C/CaO ratios**

For accurate thermal treatment and analysis, each 150 g category was further split into 25 sub-samples of 6 g each using a 6 mm spacing riffle splitter.

Table 3. Blending masses and elemental analysis of the original blended samples

Category No	Mass Pyrite (g)	Mass lime(g)	Mass coal (g)	Moles C/ CaO	CaO	C (%)
1	150.000	0.000	0.000	-	0.000	0.000
2	105.042	44.958	0.000	0.000	29.373	0.000
3	110.619	19.691	19.691	2.667	12.864	7.351
4	115.920	13.446	20.634	4.092	8.785	7.703
5	118.484	10.427	21.090	5.394	6.812	7.874
6	97.784	34.811	17.406	1.333	22.743	6.498
7	103.878	27.632	18.491	1.784	18.053	6.903

Table 4. Mineral composition of the original blended samples

Category No	FeS_2 (%)	Fe_2O_3 (%)	$CuFeS_2$	ZnS	Theoretical loss (%)
1	89.818	0.103	0.361	0.035	23.977
2	62.832	7.865	0.268	0.028	16.774
3	66.242	8.215	0.158	0.043	17.675
4	69.373	10.303	0.231	0.046	18.515
5	70.844	11.387	0.330	0.051	18.915
6	58.495	9.307	0.233	0.039	15.615

The sub-samples were precisely weighed using a RADWAG WAI ELEKTRONICZNE Model AS 60/220/C/2 electronic balance and loaded into 5.9 cm³ zirconium crucibles, which were securely covered to prevent contamination and oxidation before thermal treatment. A schematic representation of the sample preparation process is shown in Figure 3.

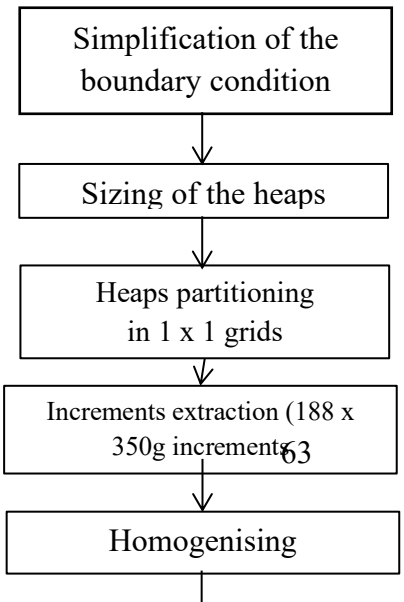

Figure 3: Sample Preparation Flow Chart

2.3. Thermal Treatments and Reduction Process

All experiments were conducted in a Nabertherm N300 muffle furnace, with strict temperature and time controls. Air circulation was discontinued by closing the airflow gate before sample introduction. Each crucible containing 6 g of the prepared sample was subjected to one of the three target temperatures: 1273 K, 1373 K, or 1473 K, with a controlled heating rate of 5 K/min.

The samples were exposed to their respective target temperatures for one of the five treatment durations: 5, 10, 15, 20, or 25 minutes. After thermal exposure, each sample was carefully removed, rapidly cooled in ambient air, weighed immediately, and stored in airtight plastic bags inside a desiccator to prevent moisture absorption and oxidation.

2.4. Data Analysis and Gravimetric Characterization

The effectiveness of pyrite decomposition, ion exchange, and carbothermic reduction was evaluated through mass percent reduction, determined using the initial and final sample masses. The mass loss was primarily attributed to the evolution of SO_2 gas, direct reduction of iron oxides, and possible side reactions.
Statistical analyses included:

(a) Pearson Correlation Test – This test was conducted to assess the correlation between mass percent reduction and independent variables (treatment temperature, duration, and composition).
(b) T-Test and Probability Value (p-value) – The t-test was used to determine the significance of mass variations, while the p-value was used to evaluate whether the null hypothesis (no significant effect of treatment) could be rejected.

3. RESULTS AND DISCUSSION

3.1. Particle Size Analysis and Sample Characterization

The particle size analysis of the pyrite concentrate samples indicated a P_{84} value of 37.75 µm, implying that 84% of the material was finer than 37.75 µm (Figure 4). The samples were not subjected to further grinding after flotation, and any replication of the analysis should adhere to the same methodology used in this study. The observed finer particle size is likely a consequence of natural degradation due to prolonged storage, as well as rolling and homogenization procedures that were employed to break up agglomerates formed during storage.

The fine particle size increases the specific surface area, which enhances reaction kinetics during thermal treatment, as reported in previous studies on iron ore reduction (Sun, 2009). However, fine particles also reduce the efficiency of magnetic separation, which could impact downstream processing. Nonetheless, since the material does not require additional grinding, its direct treatment improves cost-effectiveness in iron production. The sample characterization confirmed that the initial composition was dominated by iron (40.75%) and sulphur (48.04%), with minimal copper (0.11%) and other trace elements, as indicated in Table 1.

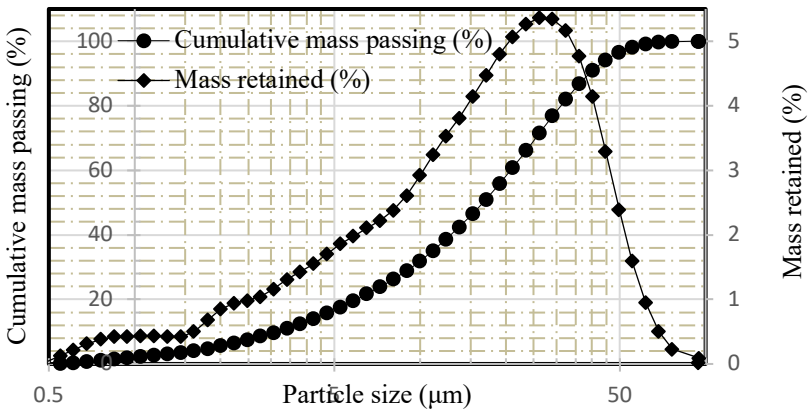

Figure 4. Particle size distribution of pyrite concentrate

3.2. Thermal Decomposition of Pyrite

3.2.1 Mass Percent Reduction and Kinetics

The mass percent reduction for pyrite thermal decomposition was determined based on the weight loss, following Equations (9) and (10), and plotted as a function of time at different temperatures (Figure 5). The Integral Method of Metallurgical Kinetics (Han, 2002) was applied to determine the reaction order by plotting actual sulphur concentrations against treatment time and fitting a linear regression using the least squares method. The Pearson correlation test was conducted to evaluate the relationship between sulphur content represented in Table 5 and mass reduction plotted in Figure 5, and the test demonstrated a strong correlation.

Table 5: Iron and sulphur content of the sample treated at different temperatures against time

Temperature (K)	Sulphur content (%)				
1273	5.45	2.3	3.23	2.24	3.12
1373	2.13	2.77	3.63	7.47	0
1473	0	0	0	0	0

A kinetic analysis was performed by plotting $\mathbf{X_S}$, $\mathbf{ln(1 - X_S)}$ and $\frac{\mathbf{X_S}}{\mathbf{1-X_S}}$ against time, where $\mathbf{X_S}$ denotes the mole fraction of sulfur measured at various temperatures over time, based on Table 5. The best-fit linear trend was selected based on the highest Pearson correlation coefficient. In this case, the plot of $\mathbf{ln(1 - X_S)}$, versus treatment time exhibited the strongest linear correlation, indicating a first-order reaction with respect to sulfur, this finding agreed with Li (2015) and Tian (2022). The rate constants were determined from the slope of the linear regression lines as follows: 0.002 at 1273 K, –0.0002 at 1373 K, and 0 at 1473 K. The activation energy ε was calculated based on the Arrhenius equation to be 0.586.
The Analysis of Variance (ANOVA) test at a 95% confidence level yielded a p-value of 0.013 as shown in Table 6, confirming that treatment time has a statistically significant effect on mass percent reduction.

Table 6: ANOVA results for the mass loss of samples at different temperature against time at the thermal decomposition reactions stage

SUMMARY	Count	Sum	Average	Variance	-	-
Row 1	5	296.4	59.28	4.812	-	-
Row 2	5	335.5	67.1	54.51	-	-
Row 3	5	364.56	72.912	7.34272	-	-
Column 1	3	196.7	65.56667	62.40333	-	-
Column 2	3	205.56	68.52	97.8492	-	-
Column 3	3	201.8	67.26667	35.89333	-	-
Column 4	3	193.5	64.5	134.59	-	-
Column 5	3	198.9	66.3	22.23	-	-

ANOVA					-	-
Source of Variation	SS	df	MS	F	P-value	F crit
Rows	467.9386	2	233.9693	7.864742	0.012918	4.45897
Columns	28.66576	4	7.16644	0.240896	0.907338	3.837853
Error	237.9931	8	29.74914			
Total	734.5975	14				

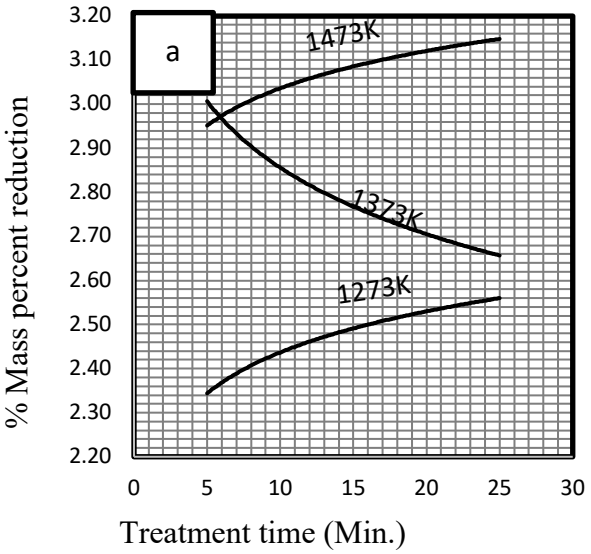

Figure 5. Mass percent reduction against time at different temperatures, at thermal decomposition. Denis (2015)

3.2.2 Effect of Temperature on Thermal Decomposition

The effect of temperature on mass percent reduction is shown in Figure 5. The mass percent reduction increased with treatment time at 1273 K and 1473 K, whereas an opposite trend was observed at 1373 K. The most significant mass loss was recorded at 1473 K, reaching a maximum of 304%, as shown in Figure 5a. The higher temperature curves consistently lay above the lower temperature ones, indicating that mass percent reduction is faster at higher temperatures.

This trend aligns with established principles of pyrite thermal decomposition, where FeS_2 decomposes into FeS and elemental sulphur (S_2) above 1016 K (Sun, 2009). Additionally, the decomposition of $FeSO_4$ and $Fe_2(SO_4)_3$ at elevated temperatures contributes to mass loss (Denis, 2015). The mass loss at 1373 K was lower, possibly due to the formation of a liquid phase, which hindered material diffusion and slowed down reaction kinetics. Thermal decomposition reactions obey the shrinkage core kinetic model which depends on the interfacial reactions, gaseous diffusion, and mass transfer through the gaseous boundary layer (Abzalov, 2008. Ying, 2013).

At the beginning of the heating process, SO_2 evolution was observed, reducing oxygen partial pressure (pO_2) to levels where elemental sulphur (S_2) started forming. The presence of liquid phases, as indicated by the Fe-S-O phase diagram (Figure 6), is likely responsible for the slower reaction kinetics at 1373 K. At 1473 K, the phase diagram shows two coexisting phases (liquid

and fcc Fe), with no gas evolution, which explains the constant mass loss despite prolonged melting time.

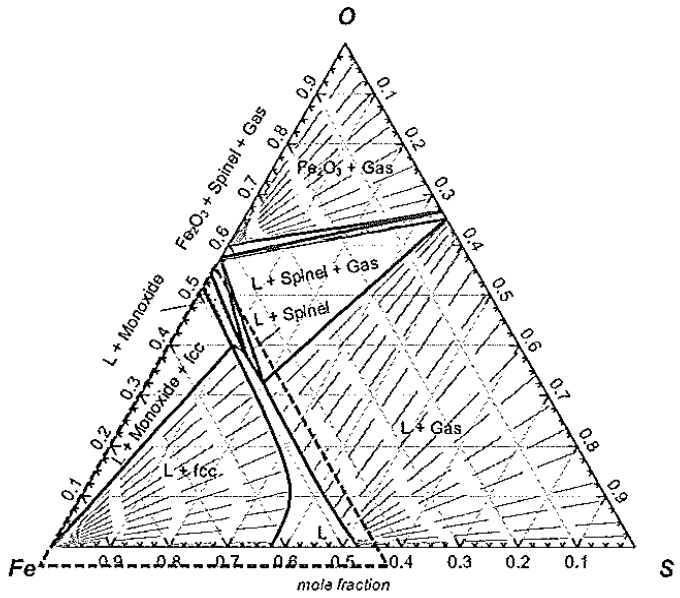

Figure 6. Isothermal section of the Fe-S-O phase diagram at 1 atm and 1200^{O}C. Denis (2015)

3.3. Ion Exchange Reactions

3.3.1. Mass Reduction Trends

At the ion exchange stage, 62.832% pyrite (FeS_2) and 29.373% CaO (lime) were mixed, and the mass percent reduction was plotted against treatment time at different temperatures (Figure 7).

The results indicate that mass loss increased at 1273 K and 1373 K, whereas at 1473 K, mass loss decreased with increasing treatment time. This behavior suggests that at lower temperatures, a significant portion of the pyrite decomposes before reacting with lime, whereas at higher temperatures, lime reactions dominate, capturing sulphur as calcium sulphide (CaS). This reverses the mass loss trend due to the retention of sulphur in the solid phase.

The regression analysis and the Integral Method of Metallurgical Kinetics similar to that described in Section 3.2.1—was applied to determine the reaction order. Plots of X_S, $\ln(1 - X_S)$ and $\frac{X_S}{1-X_S}$ versus treatment time yielded varying Pearson correlation coefficients across different temperatures. The Table 7 presents both the experimental sulphur concentrations and the corresponding correlation coefficients, with the highest value recorded at 90.79 at 1373K. This result indicates that the ion exchange reaction follows first-order kinetics with respect to sulphur at 1373 K. However, at other temperatures, the reaction order remains uncertain.

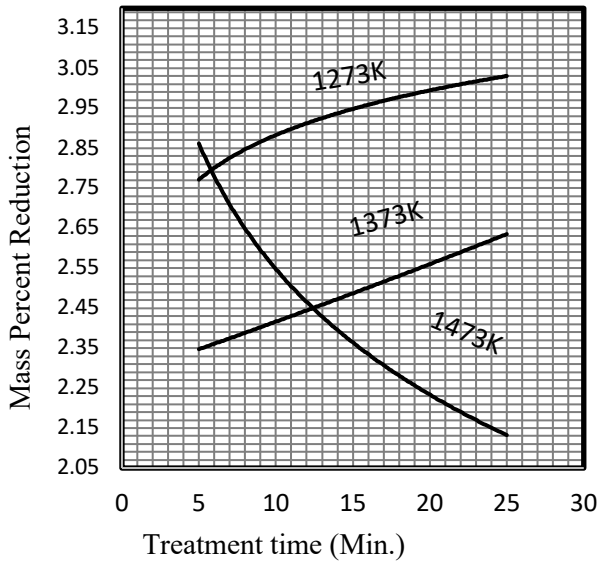

Figure 7. Mass percent reduction against time at different temperatures, at ion exchange stage

Table 7: Experimental sulfur concentrations and Pearson correlation coefficients ate various temperatures

Temperature (K)	Sulphur content (%)					Pearson Correlation Coefficient		
	5	10	15	20	25	Zero order	Fist order	Second order
1273	9.10	8.66	9.54	9.27	9.79	0.5435	0.4736	0.4387
1373	9.26	6.87	8.87	4.67	4.67	0.7475	**0.9079**	0.9020
1473	8.10	7.37	8.10	8.84	8.78	0.6823	0.4371	0.3809

3.3.2. Effect of Lime on Ion Exchange Reactions

The mass loss at 1273 K was higher than at 1373 K and 1473 K, consistent with previous findings (Hara, 2013) that showed flatter mass loss trends above 500 seconds. The dominant reaction at 1473 K was the formation of CaS from SO_2 and lime, as illustrated in Equations (5), (6), and (7).

Additionally, lime acted as a flux, lowering the melting point and leading to increased liquid formation. This liquid phase surrounded the FeS grains, hindering gas diffusion and reducing the evolution of SO_2 from the reaction center. Consequently, mass losses at the ion exchange stage were lower than those at the thermal decomposition stage due to sulphur retention in the solid phase as well as the lower melting point of the sample in the presence of lime.

The ANOVA confidence level was below 95%, implying a random distribution of mass loss data. This randomness is attributed to the heterogeneous nature of solid–solid reactions (Equations 6, 7, 13) and solid–gas reactions (Equation 8). The FeS–CaO reactions are particle-size dependent and require atomic migration between grains, which follows a probabilistic distribution (Zheng, 2012).

Furthermore, the CaO-S_2 reactions occur at phase boundaries, involving simultaneous mass and heat transfer between the reaction interface and the bulk phase. Their rate is highly dependent on the geometry and structure of CaO, which changes dynamically during the reaction. The rate-controlling step varies with reaction conditions, further contributing to the random behavior observed in mass loss trends.

3.4. Mass Percent Reduction at Pyrite Carbothermic Reduction Stage

At this stage, samples containing different ratios of pyrite, calcium oxide (CaO), and coal (C) were subjected to carbothermic reduction. The overall chemical reactions governing the process are third-order reactions, influenced by temperature, treatment time, and reactant composition. The mass percent reduction was analyzed to assess the extent of iron metallization and the role of sulphur capture in solid residues.

3.4.1. Effect of Lime Content on Mass Percent Reduction

The variation of mass percent reduction with treatment time at different lime contents is illustrated in Figure 7(a–c). The Analysis of Variance (ANOVA) test at a 95% confidence interval yielded a p-value of 2.07×10^{-5}, which is significantly below the confidence level, confirming that both treatment time and lime content had a substantial effect on mass percent reduction across all temperatures (1273 K, 1373 K, and 1473 K).

At 1273 K (Figure 8a), mass percent reduction increased with time for lime contents of 6.86% and 18.05%, while at 22.67%, the trend flattened. However, for intermediate lime contents (8.87% and 12.82%), mass percent reduction decreased with time. This variation suggests a trade-off between CO and S_2 evolution and the simultaneous capture of sulphur in the solid phase, as described by Hara (2013).

The rising trend in mass reduction is associated with gas evolution, as governed by pyrite thermal decomposition (Reaction 10), ion exchange reactions (Reaction 6), and carbothermic reduction (Reaction 5, 19). Pyrite decomposes between 683 K and 1016 K, generating elemental sulphur (S_2), which partially escapes the reaction environment, contributing to an increase in mass percent reduction (Liu, 2023).

In contrast, the flattening or declining trend at higher lime contents is attributed to the capture of sulphur as CaS (Reaction 7) as suggested by Ahindra (2008), which retains sulphur in the solid residue rather than releasing it as a gas. Additionally, the Boudouard reaction (Reaction

2), which converts CO_2 into CO, leads to further gas retention, decreasing mass loss. The mass percent reduction at carbothermic reduction stage is much less than the one at thermal decomposition stage, this could be due to smaller molar mass of carbon monoxide compared to sulphur. The lower lime content curves are higher than the high lime content, suggesting that the more lime in sample, the lower the mass loss during treatment, this is consistent with the lime desulphurization ability (Reaction 10).

3.4.2. Mass Percent Reduction at 1373 K

At 1373 K (Figure 8b), mass percent reduction generally decreased over time, except for the 18.05% lime content, where the trend was reversed. This observation suggests that thermal decomposition reactions (Reaction 10) were completed earlier at this temperature, shifting the process towards ion exchange and carbothermic reduction reactions. The increasing CO partial pressure at this stage promotes reactions (15–18), where iron oxides are reduced, leading to CO_2 formation. However, the CO_2 is partially retained in the reaction environment due to the Boudouard reaction (Reaction 2), leading to lower overall mass percent reduction.

Furthermore, lime addition promoted sulphur retention, reinforcing the decreasing mass loss trend. The inverse behavior observed at 18.05% lime content suggests a localized reaction acceleration, likely influenced by variations in sample porosity and reaction kinetics.

3.4.3. Mass Percent Reduction at 1473 K

At 1473 K (Figure 8c), the majority of curves exhibited a rising trend, though the slope flattened as lime content increased. This pattern suggests that gas evolution persisted across all three reaction stages (thermal decomposition, ion exchange, and carbothermic reduction), driven by reactions (6, 8, 10, 12, 14–18, 20). However, the flattening of curves at higher lime contents is linked to:

(a) Increased sulphur capture as CaS (Reaction 7), reducing gas evolution.
(b) Formation of liquid phases, which hinder reactant diffusion and gas release, thereby slowing the reaction kinetics.
(c) Combined effects of iron oxide reduction and the Boudouard reaction**,** where CO and $\mathbf{CO_2}$ retention further suppress mass loss.

Lime's role in lowering the melting point of the system contributes to increased liquid formation, altering the reaction pathway from solid–solid and solid–gas reactions to solid–liquid and liquid–gas interactions. This transition reduces reactant mobility, slows down gas evolution, and decreases overall mass percent reduction.

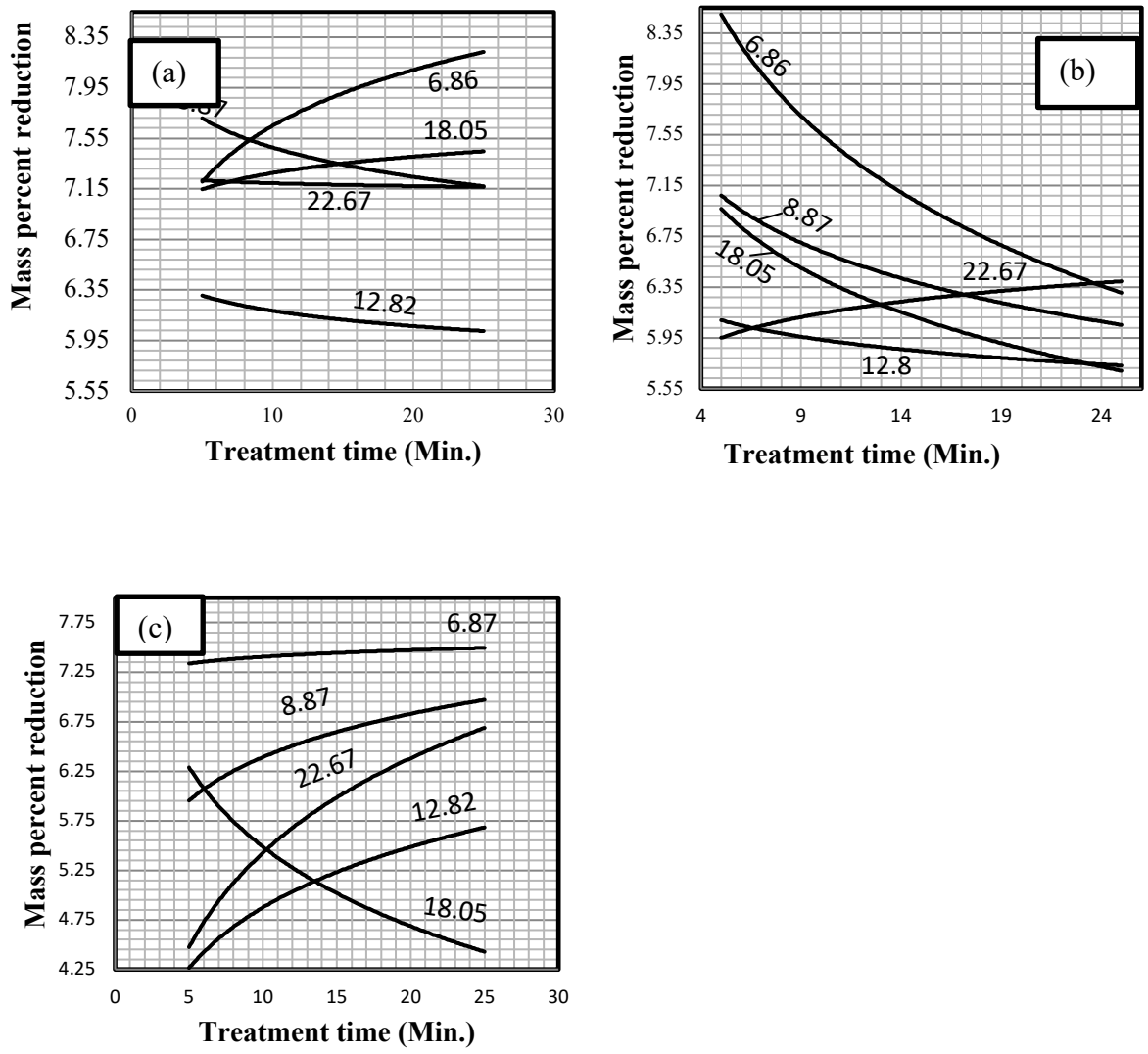

Figure 8. Percent mass reduction against treatment time and different lime contents; (a) at 1273 K; (b) at 1373 K; (c) at 1473 K

3.5. Mass Percent Reduction Against C/CaO Ratio at Different Treatment Times

3.5.1. Mass Reduction at 1273 K

The mass percent reduction as a function of the C/CaO ratio at 1273 K is plotted in Figure 9a. The trends indicate a slight decline for treatment times of 5 and 15 minutes, whereas for other treatment times, a rising trend was observed.

Since the C/CaO ratio influences the reducing capacity of the system, higher values correspond to a greater reduction potential. The increase in mass percent reduction can be attributed to enhanced activation of the Boudouard reaction (Reaction 2, 12). At this stage, solid–solid reactions (Reaction 14) dominate, where carbon reacts with iron oxides to generate CO and CO_2, leading to significant mass loss.

The decreasing trend at specific treatment times is consistent with the onset of indirect reductions, where CO_2 is increasingly retained within the reaction environment. This shift suggests that early-stage direct reductions transition into CO-mediated indirect reductions, reducing overall gas escape and mass loss.

3.5.2. Mass Reduction at 1373 K

The mass percent reduction against C/CaO ratio at 1373 K is shown in Figure 9b. Except for the 20-minute treatment time, all curves exhibited an increasing trend.

The increasing mass percent reduction is linked to the intensification of carbothermic reduction reactions (Reaction 2, 12, 14, 19). However, the flattening trend at higher C/CaO ratios suggests the acceleration of indirect reactions (Reaction 15–18), where CO and CO_2 retention begins to impact overall mass loss.

Compared to 1273 K, the mass percent reductions at 1373 K were lower, likely due to the impact of liquid phases, which inhibit reactant diffusion and slow down reaction kinetics.

3.5.3. Mass Reduction at 1473 K

The mass percent reduction against C/CaO ratio at 1473 K is plotted in Figure 9c. Here, all curves followed a rising trend, indicating a continuous increase in mass percent reduction with a higher C/CaO ratio.

This behavior is associated with the increased activation of carbothermic reduction reactions at high temperatures, particularly solid–solid reactions (Reaction 14) and iron oxide reduction reactions (Reaction 2, 5, 12, 14, 19). However, the impact of the Boudouard reaction was still evident, as retained CO_2 and CO in the reaction environment affected overall mass loss trends. Compared to 1273 K, mass reductions at 1473 K were significantly lower, reinforcing the hypothesis that liquid phases reduced reaction kinetics by limiting reactant diffusion. Additionally, the demarcated behavior of the 10-minute treatment curve suggests a distinct shift in reaction dominance, where ion exchange reactions succeeds thermal decomposition before carbothermic reduction, altering the mass loss pathway.

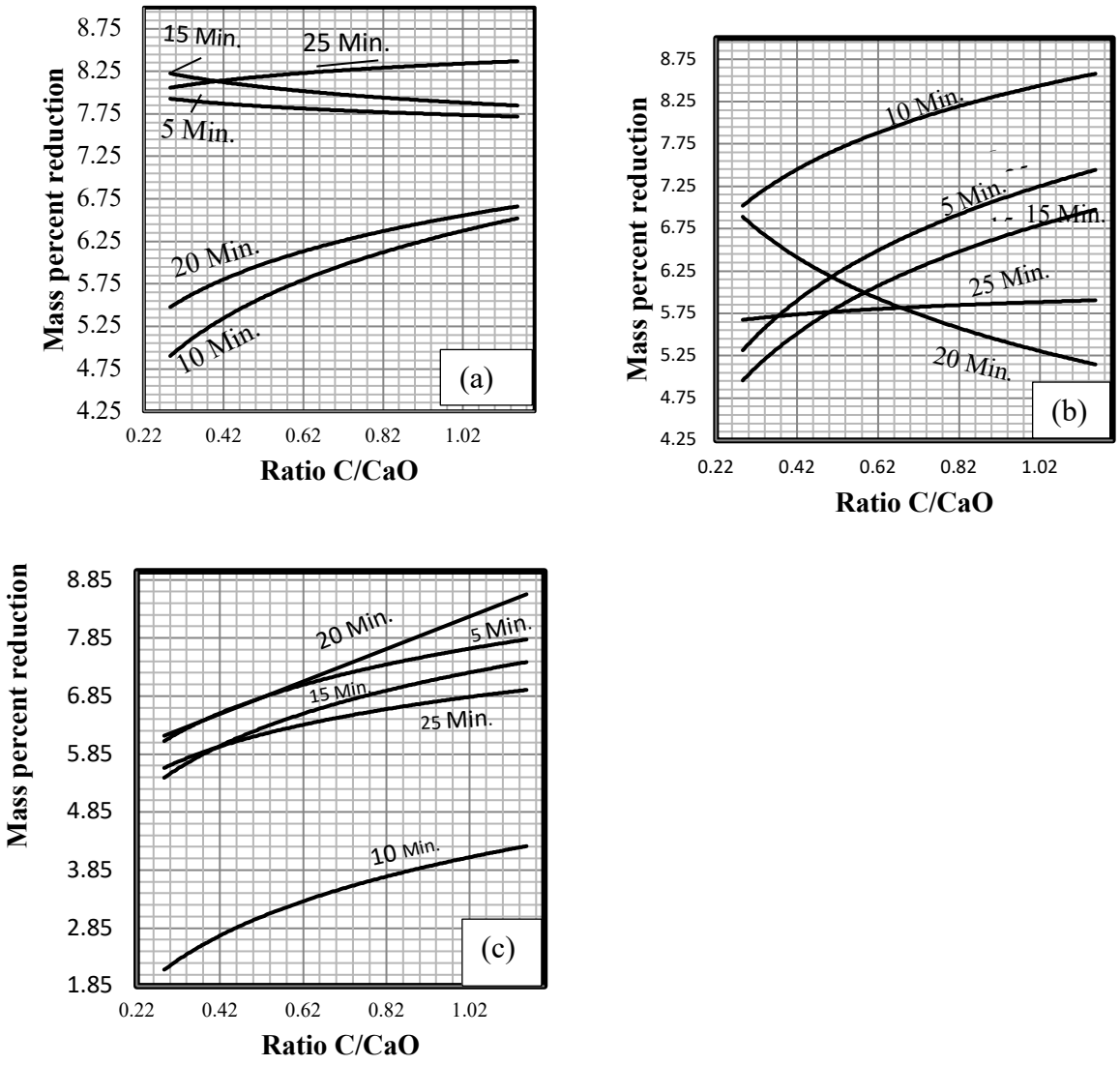

Figure 9. **Mass loss against ratio C/CaO at different treatment times for the sample treated; (a) at 1273 K, (b) at 1373 K, (c) at 1473 K**

4 CONCLUSIONS

This study investigated the carbothermic reduction of pyrite in the presence of lime, focusing on iron metallization, sulphur capture, and reaction kinetics. The results demonstrate that temperature, lime content, and the C/CaO ratio significantly influence the reduction process, affecting both metallization efficiency and sulphur retention.

Thermal decomposition exhibited the highest mass percent reduction, attributed to rapid sulphur volatilization, especially within the first five minutes of treatment. The ion exchange reaction effectively captured sulphur in the solid phase as CaS, minimizing SO_2 emissions and making the process environmentally viable. At the carbothermic reduction stage, iron metallization was enhanced at higher temperatures, though liquid phase formation hindered reaction kinetics by restricting gas diffusion. The C/CaO ratio played a crucial role, as higher ratios promoted increased metallization but also altered the balance between direct and indirect reduction mechanisms. The combined effect of iron oxide reduction and the Boudouard reaction further influenced gas retention, reducing the mass percent reduction at this stage.

The sustainability implications of these findings are significant. Recovering iron from pyrite waste while minimizing sulphur emissions aligns with global efforts to promote cleaner metallurgical processes. This approach reduces reliance on high-grade iron oxide ores, mitigates environmental pollution from pyrite cinders, and addresses acid mine drainage and air pollution concerns by capturing sulphur in a solid form. Additionally, this method provides opportunities for integrating waste-to-resource approaches in both mining and steel industries, ensuring resource efficiency and a circular economy.

Future research should focus on scaling up this process for industrial applications, further optimizing the C/CaO ratio for enhanced sulphur capture, and exploring alternative reducing agents to improve energy efficiency. Additionally, integrating waste heat recovery and by-product utilization strategies, such as using CaS in cement production for gypsum synthesis, could enhance both economic and environmental feasibility. Overall, this study provides a sustainable pathway for utilizing pyrite in iron production, contributing to a cleaner, more resource-efficient mining and metallurgy industry.

ACKNOWLEDGEMENTS

The authors acknowledge the Department of Mechanical and Metallurgical Engineering of the University of Namibia for hosting the research and the Royal Academy of Engineering for funding this project, Dr. Johannes Petrinna, Associate dean of the Faculty of Engineering and the built Environment for owning the administrative aspect of the project, Mr. Raymond Hulbert, Mr. Andrew Thomson and Mr. Craig Thomas respectively Central Operations manager, Executive Technical Director and Chief Executive Officer of Weatherly Mining Namibia for backing this project and providing samples and other relevant materials for the research.

REFERENCES

[1] Abzalov V. M., Sundai A. V., Yur'ev B. P., 2008. Desulphurization in roasting iron – Ore pellets, Steel *in Translation 38*, 1003-1007.

[2] Ahindra G., Amit C., 2008. *Ironmaking and steel making, theory and practice*, PHI Learning, New Delhi.

[3] Alpi I., Deveci H., Yazici E. Y., Türk T., Y. H. Süngün Y. H., 2009. Potential use of pyrite cinders as raw material in cement production: results of industrial scale trial operations. Journal of hazardous materials 166, 144-149.

[4] Chun T., Zhu D., Pan J., 2011. Influence of sulfur content in raw materials on oxidized pellets, Journal of Central South University of Technology *18*, 1924-1929.

[5] Denis S. Evgueni J, Sergei A., 2015. Critical Assessment and Thermodynamic Modeling of the Fe-O-S System, Journal *of Phase Equilibrium and Diffusion 36*, 224-240.

[6] Han, K.N., 2002. *Fundamentals of aqueous metallurgy*. SME.

[7] Hara, Y.S.R., 2013. Study of Reaction Mechanisms for Copper-Cobalt-Iron Sulfide Concentrates in the Presence of Lime and Carbon. *JOM*, *65*, pp.1597-1607.

[8] Hara, Y.S.R., 2014. Mineral sulphide-lime reactions and effect of CaO/C mole ratio during carbothermic reduction of complex mineral sulphides. *International Journal of Minerals, Metallurgy, and Materials*, *21*, pp.1-11.

[9] Jacobs, J.A., Lehr, J.H. and Testa, S.M., 2014. *Acid mine drainage, rock drainage, and acid sulfate soils: causes, assessment, prediction, prevention, and remediation*. John Wiley & Sons.

[10] James R. M., Julie B. Z., 2013. Environmental Engineering, fundamentals, sustainability, design. , Second ed. Florida, USA.

[11] Jiang, T., Hwang, J.Y., Alvear, G., Yucel, O., Mao, X., Sohn, H.Y., Ma, N., Mackey, P. and Battle, T. eds., 2020. *11th international symposium on high-temperature metallurgical processing*. Springer

[12] Kama M., Kama N., Leki P., 2021. Production of Sponge Iron from the Ok Tedi Pyrite concentrates, *International Journal of Science and Academic Research 2*, 1451-1455.

[13] Kutney, G., 2023. *Sulfur: history, technology, applications and industry*. Elsevier.

[14] Li, X., Chen, Z., Chen, X., Zhang, Y. and Niu, Y., 2015. Effects of mechanical activation methods on thermo-oxidation behaviors of pyrite. *Journal of Wuhan University of Technology-Mater. Sci. Ed.*, *30*(5), pp.974-980.

[15] Liu Z. C., Zheng Y., *2011.* Hexagonal hematite platelets synthesized from pyrite cinders by hydrothermal process. Journal of Central South University of Technology *18*, 1377-1382.

[16] Liu, Z.J., Xing, X.D., Zhang, J.L., Cao, M.M., Jiao, K.X. and Ren, S., 2012. Reduction mechanisms of pyrite cinder-carbon composite pellets. *International Journal of Minerals, Metallurgy, and Materials*, *19*(11), pp.986-991.

[17] Liu, L., Liu, Q., Zhang, K., Zhang, S., Li, K., Li, J. and Peng, G., 2023. Thermal decomposition and oxidation of pyrite with different morphologies in the coal gangue of North China. *Journal of Thermal Analysis and Calorimetry*, *148*(5), pp.2023-2038.

[18] Lu, L. ed., 2022. *Iron ore: mineralogy, processing and environmental sustainability*. Elsevier.

[19] Maslin, M., Van Heerde, L. and Day, S., 2022. Sulfur: A potential resource crisis that could stifle green technology and threaten food security as the world decarbonises. *The Geographical Journal*, *188*(4), pp.498-505.

[20] Qiang Z., Jilai X., Wen C.., 2019. A novel self-Magnetizing roasting process for recovering Fe from low grade pyrite cinder and blast furnace sludge, *Transition of the Indian Institute of Metals*, Technical paper, doi:10.1007/s12666-019-01724-x.

[21] Rath S. S., Rao D. S. Rao., 2017. Dolochar as a reductant in the reduction roasting of iron ore slimes*, International Journal of Minerals, Metallurgy and Materials 24*, 1341.

[22] Sun K. Lu W. K., 2009. Mathematical modelling of the kinetics of carbothermic reduction of iron oxides in ore-coal composite pellets. Metallurgical and Materials Transactions B: Process Metallurgy and Materials Processing Science *40*, 91-103.

[23] Tian, C., Rao, Y., Su, G., Huang, T. and Xiang, C., 2022. The Thermal Decomposition Behaviour of Pyrite-Pyrrhotite Mixtures in Nitrogen Atmosphere. *Journal of Chemistry*, *2022*(1), p.8160007.

[24] Vandana K., Gour G. R., Prodip S., 2015. Mathematical Model to Estimate the Rate Parameters and Thermal Efficiency for the Reduction of Iron Ore–Coal Composite Pellets in Multi-layer Bed at Rotary Hearth Furnace. *Transition of the Indian Institute of Metals 68,* 109-116.

[25] Zhang, Z., Wang, Y., He, J., Li, D., Qiu, H., Liu, F. and Lai, C., 2022. Geology, Pyrite Geochemistry and Metallogenic Mechanism of the Wulong Gold Deposit in Liaodong Peninsula, North China Craton. *Minerals*, *12*(12), p.1551.

[26] Zorya V. N., Korovushkin V. V., Permyakov A. A., Volynkina E. P., 2015. Mineral Composition and Crystalline Structure of Iron Bearing Components in Metallurgical Waste*. Steel Translation 45*, 331-337.